

Acta Crystallographica Section B

**Structural
Science**

ISSN 0108-7681

Characterization of intra-framework and guest/host interactions in the $\text{AlPO}_4\text{-15}$ molecular sieve by charge-density analysis

Emmanuel Aubert, Florence Porcher, Mohamed Souhassou and Claude Lecomte

Copyright © International Union of Crystallography

Author(s) of this paper may load this reprint on their own web site provided that this cover page is retained. Republication of this article or its storage in electronic databases or the like is not permitted without prior permission in writing from the IUCr.

Characterization of intra-framework and guest/host interactions in the AlPO_4 -15 molecular sieve by charge-density analysis

Emmanuel Aubert, Florence Porcher, Mohamed Souhassou and Claude Lecomte*

LCM3B, CNRS UMR 7036, Faculté des Sciences et Techniques, Université Henri Poincaré – Nancy I BP 239, 54506 Vandœuvre-lès-Nancy CEDEX, France

Correspondence e-mail:
lecomte@lcm3b.uhp-nancy.fr

Received 10 March 2003
Accepted 1 August 2003

The electron-density distribution of AlPO_4 -15 has been determined using high-resolution single-crystal X-ray diffraction, and the topological properties of the charge density have been calculated using the 'atoms in molecules' (AIM) theory. Analysis of the topological properties at the bond critical points has been used to characterize the interactions within the framework, and between the framework and the extra-framework species (ammonium ions and water molecules), and to define atomic properties, such as volume and net charges, uniquely. A comparison between procrystal and multipolar representations of the density was performed in order to explore to what extent the former representation is likely to reflect the interactions in the solid. Correlation with geometrical properties (P–O and Al–O bond lengths, and Al–O–P angle) is found for topological charges obtained from the multipolar model, but not for the results from the procrystal representation.

1. Introduction

The characterization of interactions between 'zeolite' frameworks and guest molecules is of great interest, as it may provide information about synthesis methods [template/SDA (structure-directing agent) effects] catalytic processes (electrophilic/nucleophilic sites) and confinement effects (spectral shifts, non-linear optics; Cheetham *et al.*, 1999). As most of these interactions are of an electrostatic nature, an accurate study of electron-density distribution is required in order to determine the electrostatic properties (electrostatic potential, field *etc.*) of the zeolite framework and of the composite. Reliable electron-density studies on such complex materials are rarely achieved with theoretical calculations because of the system size. On the other hand, high-resolution X-ray diffraction analysis is less dependant on the size of the system; such an analysis requires, however, a crystal quality that is seldom found in molecular sieves, which often grow as a fine powder or as disordered or twinned crystals. Studying dense, chemically analogous systems with good crystalline quality allows an accurate electron-density determination, whose parameters can be transferred to systems for which electron density cannot be directly determined experimentally. Such an approach of transferability for organic fragments has already been used to model large protein systems (Pichon-Pesme *et al.*, 1995; Jelsch *et al.*, 2000).

In this paper, we describe an experimental electron-density study of the AlPO_4 -15 molecular sieve, whose three-dimensional network based on PO_4 tetrahedra linked to AlO_6 octahedra exhibits small channels. In this structure, a hydroxyl

group and a structural water molecule complete one AlO_6 octahedron, while a second water molecule and a charge-compensating NH_4^+ cation lie in the channels, thus leading to small dioxygen adsorption capacities (Szostak, 1992). Deformation densities and topological properties of the P–O, Al–O and H bonds are described; finally, by comparing results issued from the experimental and procrystal models, we discuss and illustrate the necessity of using a multipolar representation of the charge density in order to analyse the P–O, Al–O and hydrogen-bonding interactions.

2. Experimental

2.1. Syntheses and characterization

$\text{AlPO}_4\text{-15}$ crystals were obtained as a pure phase using a modification of a procedure which aimed to grow AFI-type material (Weiß *et al.*, 2000). The syntheses were carried out in home-built stainless-steel autoclaves equipped with a Teflon gasket. NH_3 (25 ml, 32% in solution) was added to aluminium sulfate hexadecahydrate (6.72 g) dissolved in distilled water (100 ml), and the slurry formed was filtered overnight and washed with NH_3 solution. The resulting gel was dispersed in distilled water (65 ml), with subsequent dropwise addition of ethanol (14.20 g, 98%), with stirring, phosphoric acid (1.29 g, 85% in solution) and tripropylamine (1.38 g, 98%); the Al/P ratio of the gel was 1.87. The 130 ml-capacity reactors were filled to 75% of their volume with the gel and placed in a preheated oven at 453 K for 4 d. The reactors were then cooled in cold running water, and the reaction products were recovered by filtration, washed with distilled water and finally dried overnight at ~ 353 K. No gel remained and optical examination showed that all crystals belonged to the same species. Microprobe analyses indicate an Al/P ratio of 1.11 (8), in agreement with the expected ratio of 1 (within 2 s.u.).

2.2. X-ray diffraction experiment

A crystal was selected after optical examination and was mounted on an Mo $K\alpha$ Nonius KappaCCD diffractometer. Firstly, a rapid data collection at room temperature was made, in order to check the crystal quality and for structure determination. The high-resolution diffraction experiment for the charge-density study was then undertaken at 115 K using an Oxford Cryosystem liquid-nitrogen cooling device. The temperature of the experiment was calibrated according to the phase transition of ammonium dihydrogen phosphate (148 K; Pérès *et al.*, 1997).

Indexing and integration of Bragg intensities were performed with the *HKL2000* program package (Otwinowski & Minor, 1997). A Gaussian absorption correction (DeTitta, 1985) based on crystal habitus (Table S1 and Fig. S1¹) was applied (Table 1) before equivalent reflections were scaled and averaged using *SORTAV* (Blessing, 1997; Blessing *et al.*, 1998, and references therein). Completeness of the data was

¹ Supplementary data for this paper are available from the IUCr electronic archives (Reference: CK0023). Services for accessing these data are described at the back of the journal.

Table 1
Experimental table.

Crystal data	
Chemical formula	$\text{NH}_4\text{Al}_2(\text{OH})(\text{H}_2\text{O})(\text{PO}_4)_2 \cdot 2\text{H}_2\text{O}$
M_r	314.98
Cell setting, space group	Monoclinic, $P2_1/n$
a, b, c (Å)	9.556 (1), 9.563 (1), 9.615 (1)
β (°)	103.58 (1)
V (Å ³)	854.1 (2)
Z	4
D_x (Mg m ⁻³)	2.450
Radiation type	Mo $K\alpha$
No. of reflections for cell parameters	145 662
θ range (°)	3–49
μ (mm ⁻¹)	0.76
Temperature (K)	115 (1)
Crystal form, colour	12-faced polyhedron, colourless
Crystal size (mm)	0.22 × 0.17 × 0.14
Data collection	
Diffractometer	Nonius KappaCCD diffractometer
Data collection method	φ and ω scans
Absorption correction	Integration [<i>ABSORB</i> (DeTitta, 1985)]
T_{\min}	0.89
T_{\max}	0.93
No. of measured, independent and observed reflections	145 662, 8561, 8561
Criterion for observed reflections	$I > 0\sigma(I)$
R_{int}	0.029
θ_{\max} (°)	49
Range of h, k, l	$-19 \Rightarrow h \Rightarrow 19$ $-20 \Rightarrow k \Rightarrow 20$ $-20 \Rightarrow l \Rightarrow 19$
Refinement	
Refinement on	F
$R[F^2 > 0\sigma(F^2)]$, $wR(F)$, S	0.010, 0.007, 1.65
No. of reflections	4725
No. of parameters	510
H-atom treatment	See text
Weighting scheme	Based on measured s.u. values [$w = \sigma^{-2}(F_{\text{obs}})$]
$(\Delta/\sigma)_{\max}$	0.09
$\Delta\rho_{\max}$, $\Delta\rho_{\min}$ (e Å ⁻³)	0.20, -0.20
Extinction method	Becker & Coppens (1974)
Extinction parameter g	870

Computer programs used: *KappaCCD Software* (Nonius, 1997), *HKL2000* (Otwinowski & Minor, 1997), *DREAD* (Blessing, 1989), *NRCVAX* (Gabe *et al.*, 1989), *MoPro* (Guillot *et al.*, 2001).

attained up to $(\sin \theta/\lambda)_{\max} = 1.0 \text{ \AA}^{-1}$. Only the five lowest-resolution reflections shaded by the beam stop were not measured. The intensities of 164 negative and weak reflections were reestimated using a Bayesian probabilistic approach (Blessing, 1989). Crystal data and more experimental details are summarized in Table 1.

2.3. Structural and multipolar refinements

The low-temperature structure was solved by direct methods in space group $P2_1/n$ using *NRCVAX* (Gabe *et al.*, 1989); all H atoms were located in difference-Fourier maps. The multipolar refinements were performed using *MoPro* (Guillot *et al.*, 2001). The electron density was modelled according to the multipolar formalism of Hansen & Coppens (1978)

Table 2
Initial ξ and n_l parameters.

Atom type	ξ (bohr ⁻¹)	$n_{l=1}$	$n_{l=2}$	$n_{l=3}$	$n_{l=4}$
P	3.5	6	6	7	7
Al	2.72	4	4	4	4
O	4.5	2	2	3	–
N	3.8	2	2	3	–
H	2.28	1	–	–	–

$$\rho(r) = \rho_c(r) + P_v \kappa^3 \rho_v(\kappa r) + \sum_{l=0}^{l_{\max}} \kappa^3 R_l(\kappa' r) \sum_{m=0}^l P_{lmp} y_{lmp}(\theta, \varphi), \quad (1)$$

where $\rho_c(r)$ and $\rho_v(r)$ are the core and valence free-atom densities, P_v and P_{lmp} ($p = \pm$) are the valence and multipole populations, κ and κ' are expansion/contraction parameters, R_l are Slater type radial functions, with $R_l(r) = \xi^{n_l+3}/(n_l+2)! \times r^{n_l} \exp(-\xi r)$, and y_{lmp} are spherical harmonic functions in the real form.

The form factors of the core and valence electrons were calculated using free-atom Clementi wavefunctions (Clementi & Roetti, 1974), and a contracted H-atom form factor was used (Stewart *et al.*, 1965). Anomalous dispersion coefficients were taken from Kissel *et al.* (1995). Phosphorous- and aluminium-centred multipoles were developed up to the hexadecapole level ($l = 4$), while those of oxygen and nitrogen were developed up to octupoles ($l = 3$), and those of hydrogen were developed up to dipoles ($l = 1$). Initial n_l and ξ parameters (Table 2) were chosen according to previous work (Souhassou *et al.*, 1995; Pérès, 1997; Kuntzinger & Ghermani, 1999); atomic frames, displayed in Fig. S2, are defined according to local symmetry. In order to compute a free R -factor (Brünger, 1992), 10% of the unique reflections (randomly chosen) were not used in the least-squares fitting and were used only in the R_{free} calculation. Refinements using the *MoPro* package (Guillot *et al.*, 2001) were performed on F , with no I/σ cutoff, and the electroneutrality of the unit cell was imposed. The refinement strategy was as follows:

Step 1: Conventional independent-atom model (IAM) refinement. The scale factor, atomic positions and anisotropic atomic displacement parameters (ADPs) were refined for all non-H atoms using data with $0.80 < (\sin \theta/\lambda)_{\max} < 0.95 \text{ \AA}^{-1}$ (preliminary refinements showed that reflections at higher resolution were estimated badly). H-atom isotropic ADPs were restrained to 1.2 (1) times the equivalent ADPs of their parent atoms as programmed in *MoPro*.

Step 2: High-order refinement ($0.8 < \sin \theta/\lambda < 0.95 \text{ \AA}^{-1}$). The scale factor, atomic positions and ADPs for all heavy atoms were refined.

Step 3: H-atom refinement (x, y, z, U_{iso}) using all reflections up to $\sin \theta/\lambda < 0.95 \text{ \AA}^{-1}$. H-atom positions were then adjusted to the average neutron distances (hydroxyl group O–H = 1.00 Å, water O–H = 0.96 Å and ammonium N–H = 1.003 Å; Allen *et al.*, 1987; Pérès *et al.*, 1997).

Step 4: Secondary extinction type I (Becker & Coppens, 1974), deformation density (P_v, P_{lmp}, κ and κ'), positional and

Table 3
Agreement indices.

Step 1: spherical-atom model; step 2: high-order refinement; step 3: H-atom refinement; step 4: multipolar model; step 5: Kappa refinement (Coppens *et al.*, 1979). For each step and substep, the first line gives the indices at the end of refinement, and the second line gives the R_{free} calculations. $R = (\sum_{\mathbf{H}} ||F_{\text{obs}}| - |kF_{\text{calc}}||) / (\sum_{\mathbf{H}} |F_{\text{obs}}|)$, $R_w = \{[\sum_{\mathbf{H}} w (|F_{\text{obs}}| - |kF_{\text{calc}}|)^2] / (\sum_{\mathbf{H}} w |F_{\text{obs}}|^2)\}^{1/2}$, $\text{GoF} = \{[\sum_{\mathbf{H}} w (|F_{\text{obs}}| - |kF_{\text{calc}}|)^2] / (m - n)\}^{1/2}$, $w = \sigma^{-2}(F_{\text{obs}})$, m is the number of reflections used and n is the number of parameters.

Step	Resolution shell/ substeps	R	R_w	GoF	No. of variables	No. of observa- tions
1	$\sin \theta/\lambda < 0.95 \text{ \AA}^{-1}$	0.0186	0.0230	5.15	181	5553
		0.0171	0.0235	5.12		577
	† $0.8 < \sin \theta/\lambda < 0.95 \text{ \AA}^{-1}$	0.0249	0.0173	1.54	0	2231
		0.0238	0.0173	1.68		233
2	$0.8 < \sin \theta/\lambda < 0.95 \text{ \AA}^{-1}$	0.0210	0.0133	1.22	145	2231
		0.0191	0.0125	1.21		233
3	$\sin \theta/\lambda < 0.95 \text{ \AA}^{-1}$	0.0198	0.0266	5.87	37	5553
		0.0182	0.0229	5.16		577
4	$\sin \theta/\lambda < 0.90 \text{ \AA}^{-1}$	0.0102	0.0066	1.65	510	4725
		0.0103	0.0067	1.58		494
	† $\sin \theta/\lambda < 0.95 \text{ \AA}^{-1}$	0.0122	0.0071	1.57	0	5553
		0.0119	0.0073	1.60		577
† $\sin \theta/\lambda < 0.90 \text{ \AA}^{-1}$ and $I/\sigma > 3$		0.0082	0.0065	1.59	0	4373
		0.0082	0.0066	1.59		462
5	$\sin \theta/\lambda < 0.90 \text{ \AA}^{-1}$	0.0153	0.0163	3.88	35	4725
		0.0146	0.0160	3.73		494

† Calculation of agreement indices without refinement of the parameters.

ADP parameters were refined. In order to avoid correlations, nine sets of κ, κ' parameters were refined according to chemical equivalence, namely P, Al, bridging O, hydroxyl O and H, water O and H, and ammonium N and H atoms. Fig. 1 shows large underestimations of the observed high-angle intensities, and therefore the resolution range was further restricted to $(\sin \theta/\lambda)_{\max} < 0.90 \text{ \AA}^{-1}$, $I > 0$. Difficulties in estimating intensities and their standard deviations were also encountered in other charge-density studies performed with the Nonius KappaCCD diffractometer (Kuntzinger *et al.*, 1999). Once this cutoff had been chosen, the convergence was very robust and restraints on H-atom isotropic ADPs were successfully removed at the end of the refinement.

Step 5: A spherical-atom kappa refinement (Coppens *et al.*, 1979) was performed using the positional parameters and anisotropic ADPs obtained in step 4.

Agreement factors at different refinement steps are given in Table 3. Multipolar refinement considerably reduced the agreement indices, including the R_{free} factors, which highlights the necessity of using an aspherical-atom formalism for accurate analysis of diffraction data (R_w decreased from 0.027 to 0.007 from step 3 to step 4).

At the end of step 4, the extinction parameter refined to $g = 8.7 (5) \times 10^2$ (37.7 s); 116 reflections were slightly affected ($y_{\max} = 5\%$ for -231 and 200 *etc.*). The maximal shifts occurred for water O atoms, with $(\Delta/\sigma)[K'O] < 0.09$ and

$(\Delta/\sigma)[P_{33+O}] < 0.06$. The residual density as calculated by the equation

$$\Delta\rho_{\text{res}}(\mathbf{r}) = V^{-1} \left\{ \sum_{\mathbf{H}} [k^{-1}|F_{\text{obs}}(\mathbf{H})| - |F_{\text{calc}}(\mathbf{H})|] \times \exp(i\varphi_{\text{calc}}) \exp(-2\pi i\mathbf{H} \cdot \mathbf{r}) \right\} \quad (2)$$

has extrema of $\pm 0.20 \text{ e } \text{\AA}^{-3}$ uniformly distributed throughout the asymmetric unit (Fig. 2). These extrema are reduced to $0.05 \text{ e } \text{\AA}^{-3}$ by removing reflections with $I/\sigma < 3$ in the Fourier calculation (see Fig. S3 of the supplementary material). The maximum average error on the density is given by $\sigma(\rho) = \left\{ \sum_{\mathbf{H}} [\Delta F(\mathbf{H})]^2 \right\}^{1/2} / V_{\text{cell}}$ and is estimated to be $0.04 \text{ e } \text{\AA}^{-3}$ (with $I > 0$). A numerical check for the positivity of the total electron density was performed throughout the asymmetric unit, with a grid step of 0.04 \AA ; the smallest density was only slightly negative ($-1.5 \times 10^{-3} \text{ e } \text{\AA}^{-3}$, which is much less than the estimated errors) and was located $\sim 1 \text{ \AA}$ from atom H1 (opposite to atom O9). Fig. 3 displays the variation of agreement factors R , R_w , R_{free} and $R_{w\text{free}}$ as a function of resolution. Residual and free indices behave in the same manner, showing that no supplementary information was present in the reflections used for the free R calculation; these indices increase with resolution because of the lower signal-to-noise ratio, the smaller redundancy of high-angle reflections and scaling problems, as noticed at step 4 (in the choice of the resolution cutoff). All statistical indices and residual maps testify to the excellent quality of both the data and the charge-density model. The final positional, anisotropic ADPs and multipolar parameters

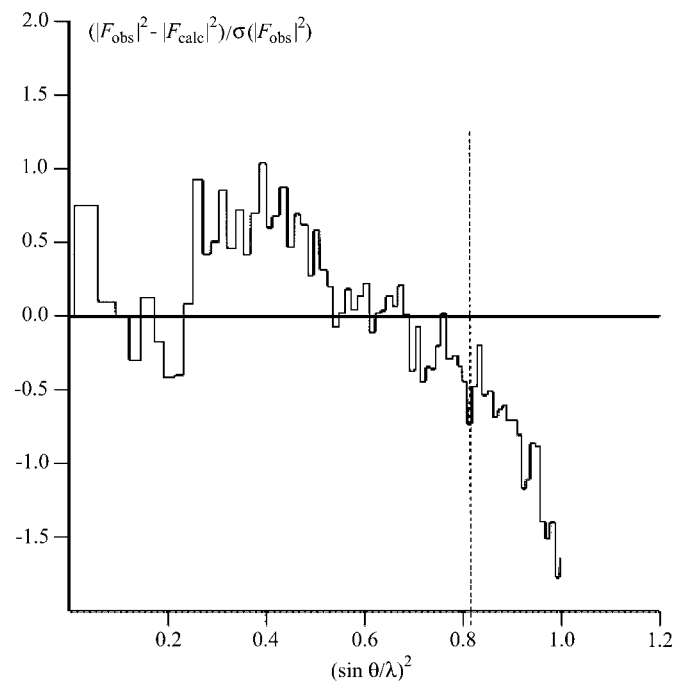


Figure 1
 $(F_{\text{obs}}^2 - F_{\text{calc}}^2) / \sigma(F_{\text{obs}}^2)$ at the end of step 4 plotted against $(\sin \theta / \lambda)^2 (\text{\AA}^{-2})$ per shell of 100 reflections. The dotted vertical line delimits the 0.9 \AA^{-1} resolution cutoff.

obtained at the end of step 4 are given as supplementary material (Tables S2 and S3).

3. Results

3.1. Crystal structure

Interatomic bond distances and angles are reported in Table 4, and an ORTEPII (Johnson, 1976) view of the structure is shown in Fig. 4(a).

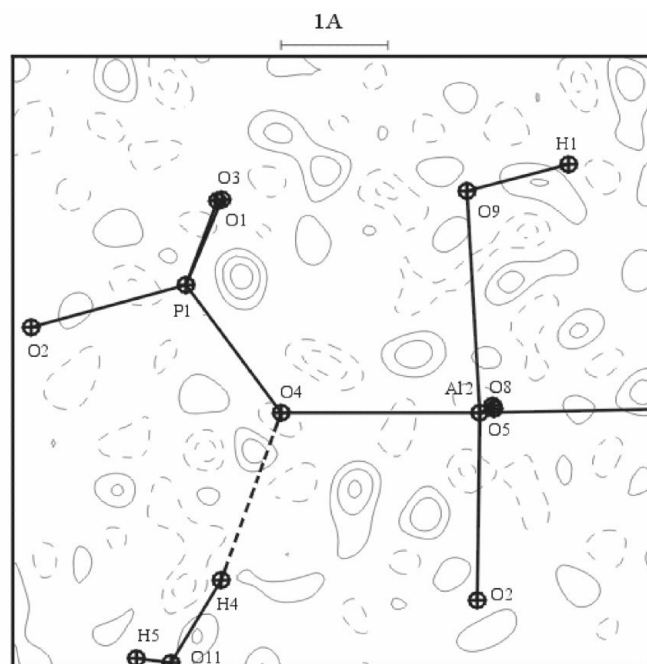


Figure 2
Residual density map at the end of the multipolar refinement in the P1–O4–A12 plane ($\sin \theta / \lambda < 0.90 \text{ \AA}^{-1}$, $I/\sigma > 0$). The contour interval is $0.05 \text{ e } \text{\AA}^{-3}$; positive contours are shown as solid lines, negative contours are shown as dashed lines and zero contours have been omitted.

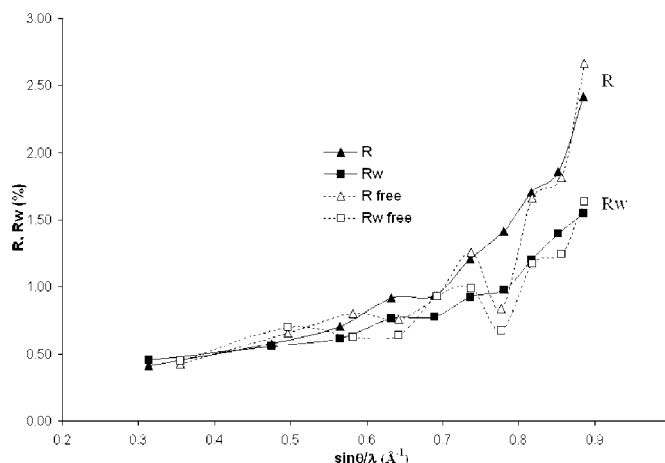


Figure 3
Statistical indices R , R_w , R_{free} and $R_{w\text{free}}$ as a function of resolution. Agreement factors are calculated in ten shells of, on average, 472 and 49 (R_{free}) reflections per shell, respectively.

Table 4

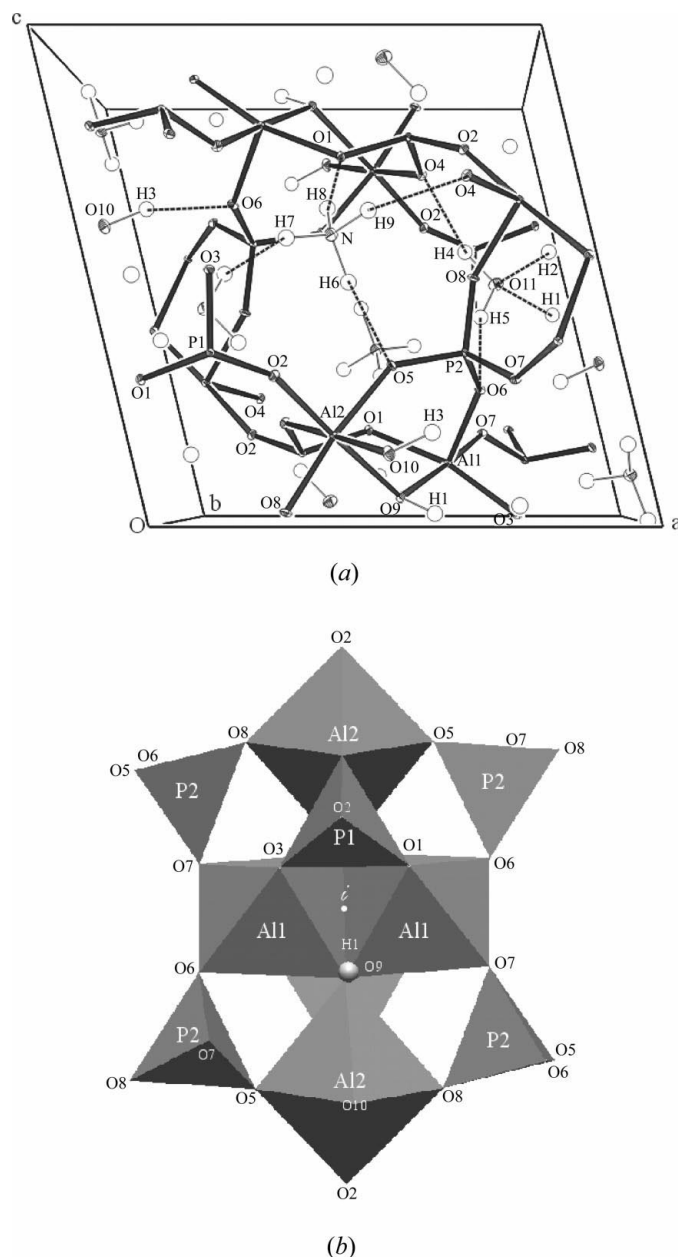
Interatomic distances (Å) and bond-valence angles (°).

P1—O1	1.5410 (2)	Al1—O1	1.8721 (3)
P1—O2	1.5101 (2)	Al1—O3	1.8716 (3)
P1—O3	1.5498 (2)	Al1—O6	1.8567 (2)
P1—O4	1.5433 (2)	Al1—O7	1.8342 (2)
		Al1—O9	2.0300 (3)
		Al1—O9	2.0479 (3)
P2—O5	1.5326 (2)	Al2—O2	1.8485 (2)
P2—O6	1.5461 (2)	Al2—O4	1.8590 (2)
P2—O7	1.5293 (2)	Al2—O5	1.8330 (2)
P2—O8	1.5204 (2)	Al2—O8	1.8254 (2)
		Al2—O9	2.1886 (3)
		Al2—O10	1.9415 (3)
O9—H1	0.987 (5)	N—H6	0.999 (4)
O10—H2	0.959 (5)	N—H7	0.999 (4)
O10—H3	0.958 (4)	N—H8	0.998 (4)
		N—H9	0.998 (4)
O11—H4	0.957 (4)		
O11—H5	0.953 (4)		
O1—P1—O2	112.36 (1)	O1—Al1—O7	91.20 (1)
O1—P1—O3	109.53 (1)	O1—Al1—O9	84.92 (1)
O1—P1—O4	109.19 (1)	O1—Al1—O3	166.58 (1)
O2—P1—O3	108.10 (1)	O1—Al1—O9	85.29 (1)
O2—P1—O4	109.09 (1)	O7—Al1—O9	176.02 (1)
O3—P1—O4	108.50 (1)	O7—Al1—O3	97.86 (1)
		O7—Al1—O9	91.94 (1)
O5—P2—O6	109.22 (1)	O9—Al1—O3	85.81 (1)
O5—P2—O7	111.34 (1)	O9—Al1—O9	86.85 (1)
O5—P2—O8	107.60 (1)	O3—Al1—O9	84.52 (1)
O6—P2—O7	108.05 (1)	O7—Al1—O6	87.02 (1)
O6—P2—O8	109.14 (1)	O6—Al1—O3	93.54 (1)
O7—P2—O8	111.47 (1)	O6—Al1—O1	96.82 (1)
		O6—Al1—O9	94.32 (1)
		O6—Al1—O9	177.66 (1)
Al1—O9—Al1	93.15 (1)	O4—Al2—O9	86.86 (1)
Al1—O9—Al2	124.63 (1)	O4—Al2—O10	178.32 (1)
Al2—O9—Al1	123.19 (1)	O4—Al2—O2	89.26 (1)
Al1—O9—H1	107.6 (3)	O4—Al2—O8	94.20 (1)
Al2—O9—H1	102.2 (3)	O9—Al2—O10	91.98 (1)
H1—O9—Al1	104.2 (2)	O9—Al2—O2	174.81 (1)
		O9—Al2—O8	90.20 (1)
H6—N—H7	108.7 (3)	O10—Al2—O2	91.97 (1)
H6—N—H8	110.4 (4)	O2—Al2—O8	93.52 (1)
H6—N—H9	106.3 (3)	O5—Al2—O2	90.03 (1)
H7—N—H8	114.1 (3)	O5—Al2—O4	93.74 (1)
H7—N—H9	112.5 (3)	O5—Al2—O10	87.40 (1)
H8—N—H9	104.5 (3)	O8—Al2—O5	171.34 (1)
		O5—Al2—O9	86.79 (1)
		O10—Al2—O8	84.59 (1)
P1—O1—Al1	126.33 (1)	Al2—O10—H2	116.7 (3)
P1—O2—Al2	157.12 (1)	Al2—O10—H3	131.6 (2)
P1—O3—Al1	126.34 (1)	H2—O10—H3	109.2 (4)
P1—O4—Al2	125.24 (1)	P2—O8—Al1	146.64 (1)
P2—O5—Al2	140.35 (1)		
P2—O6—Al1	133.18 (1)		
P2—O7—Al1	134.80 (1)		
P2—O8—Al2	146.64 (1)		

The three-dimensional structure of $\text{AlPO}_4\text{-15}$ consists of sheets, parallel to the $(10\bar{1})$ plane, that are linked *via* O2 atoms [$\text{P1—O2—Al2} = 157.12 (1)^\circ$]. A sheet contains two crystallographically independent AlO_6 octahedra linked *via* PO_4 bridges (see Fig. 4*b*); the Al1O_6 octahedron is connected to four PO_4 tetrahedra through atoms O1 and O3 (P1), and O6 and O7 (P2). Two Al1O_6 octahedra related by an inversion centre share one edge through two hydroxyl groups, each of which is also coordinated to an Al2O_6 octahedron. The Al2O_6 octahedron is linked to the PO_4 tetrahedra, *via* atoms O2 and O4 (P1), and O5 and O8 (P2), and to one water molecule

(atom O10). The O10—Al2 distance is short [1.9415 (3) Å] compared with the Al2—O(—H) distance [2.1886 (3) Å].

The P1O_4 and P2O_4 tetrahedra are almost undistorted, unlike the AlO_6 octahedra, which are bound to three O-atom types (bridging, hydroxyl and water), with Al—O bonds ranging from 1.8254 (2) (bridging oxygen) to 2.1886 (3) Å (hydroxyl atom O9). The O—Al—O angles are also substantially distorted [$\text{O7—Al1—O3} = 97.86 (1)^\circ$, $\text{O3—Al1—O9} = 84.52 (1)^\circ$ and $\text{O1—Al1—O3} = 166.58 (1)^\circ$]. Similar distortions are observed in isostructural leucophosphate compounds (Dick & Zeiske, 1997; Nandini Devi & Vidyasagar, 1999; Beitone *et al.*, 2002).

**Figure 4**

(a) ORTEPII (Johnson, 1976) plot of the $\text{AlPO}_4\text{-15}$ structure. Ellipsoids are plotted at the 50% probability level and hydrogen bonds with $\text{H} \cdots \text{A} < 2.08 \text{ \AA}$ are plotted as dashed lines. (b) Polyhedral representation of the structure. An inversion centre, *i*, lies in the centre of this figure.

The $\text{AlPO}_4\text{-15}$ framework contains small elliptical channels of $3.5 \times 4.7 \text{ \AA}$, which lie parallel to the **b** axis and which are filled by an ammonium ion and a non-structural water molecule, thus leading to 23 host–host and host–guest $\text{H}\cdots\text{O}$ contacts of less than 2.7 \AA . Nine contacts fall in the range $1.76\text{--}2.08 \text{ \AA}$, with $\text{O}\cdots\text{H}\text{--}X$ angles larger than 152° , and there are 14 longer contacts in the range $2.48\text{--}2.70 \text{ \AA}$ ($\text{O}\cdots\text{H}\text{--}X < 123^\circ$). The ammonium ion is connected to the framework

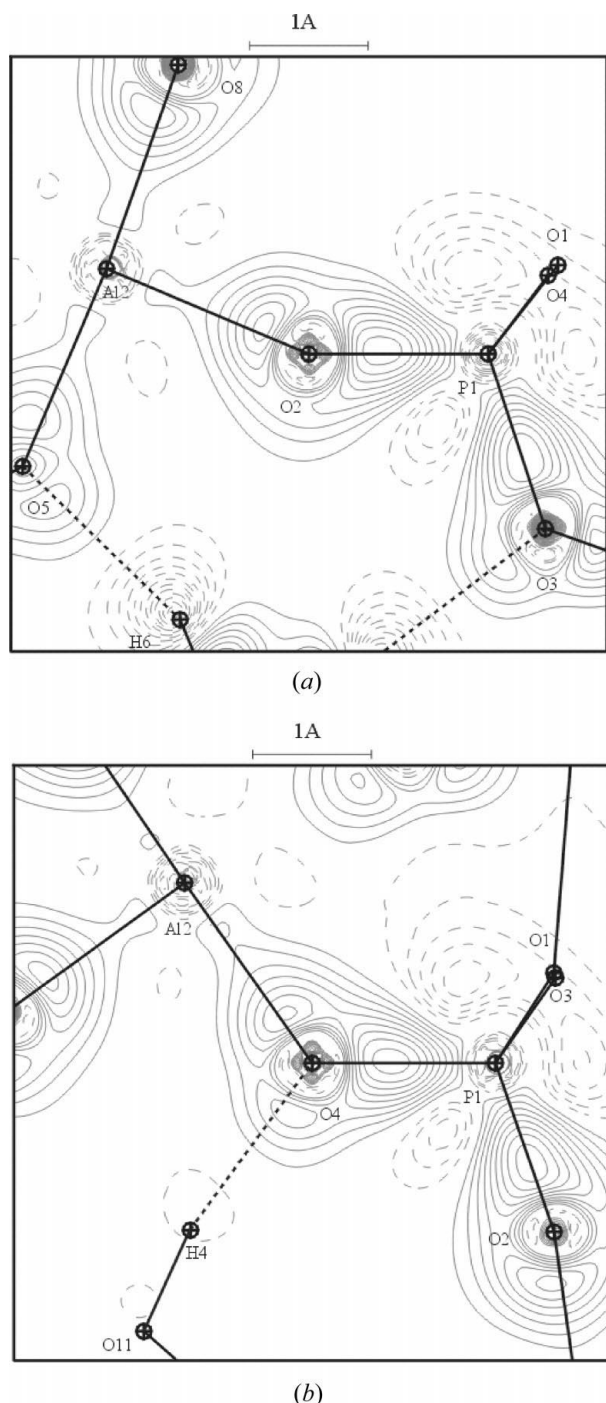


Figure 5
Static deformation maps. (a) $\text{Al2}\text{--O2}\text{--P1}$ plane. (b) $\text{Al2}\text{--O4}\text{--P1}$ plane. Contours as in Fig. 2.

Table 5

Geometric characteristics (\AA , $^\circ$) of $D\text{--H}\cdots A$ contacts defined as hydrogen bonds [contacts for which a (3,–1) BCP was found between the H atom and the acceptor atom].

$D\text{--H}\cdots A$	$D\text{--H}$	$\text{H}\cdots A$	$D\cdots A$	$D\text{--H}\cdots A$
$\text{O10--H2}\cdots\text{O11}$	0.959 (5)	1.758 (5)	2.7013 (4)	167.2 (4)
$\text{N--H8}\cdots\text{O1}$	0.998 (4)	1.815 (4)	2.7950 (4)	166.2 (3)
$\text{N--H6}\cdots\text{O5}$	0.999 (4)	1.869 (4)	2.8615 (4)	172.1 (4)
$\text{O11--H4}\cdots\text{O4}$	0.957 (4)	1.882 (4)	2.8147 (3)	164.2 (4)
$\text{N--H7}\cdots\text{O3}$	0.999 (4)	1.883 (4)	2.8564 (4)	163.9 (3)
$\text{O10--H3}\cdots\text{O6}$	0.958 (4)	1.901 (4)	2.8230 (3)	160.7 (3)
$\text{N--H9}\cdots\text{O4}$	0.998 (4)	2.005 (4)	2.9298 (4)	152.9 (3)
$\text{O9--H1}\cdots\text{O11}$	0.987 (5)	2.037 (5)	3.0190 (4)	172.9 (4)
$\text{O11--H5}\cdots\text{O6}$	0.953 (4)	2.071 (4)	2.9816 (4)	159.5 (3)
$\text{O10--H3}\cdots\text{O7}$	0.958 (4)	2.485 (4)	3.1074 (4)	122.6 (3)
$\text{N--H6}\cdots\text{O2}$	0.999 (4)	2.488 (4)	3.0216 (4)	113.0 (3)
$\text{O11--H4}\cdots\text{O2}$	0.957 (4)	2.488 (5)	3.0437 (4)	116.9 (3)
$\text{N--H8}\cdots\text{O7}$	0.998 (4)	2.565 (4)	3.1635 (4)	118.3 (3)
$\text{O11--H5}\cdots\text{O7}$	0.953 (4)	2.664 (4)	3.250 (4)	120.3 (4)

O atoms *via* its four H atoms ($\text{H}\cdots\text{O}$ ranging from 1.8 to 2.1 \AA). The free water molecule interacts with the framework through both its H and its O atoms. The resulting contacts are fully characterized by the topological analysis of the charge density (§3.6).

3.2. Deformation densities

The static deformation density, which is defined as the difference between the total electron density and the procrystal density, gives the electron redistribution due to chemical bonding and interatomic interactions

$$\Delta\rho(r) = P_v \kappa^3 \rho_v(\kappa r) - N_v \rho_v(r) + \sum_{l=0}^{l_{\max}} \kappa'^3 R_l(\kappa' r) \sum_{m=0}^l P_{lmp} Y_{lmp}(\theta, \varphi). \quad (3)$$

Static deformation-density maps were calculated using *SALLY* (Hansen, 1998).

As shown in Figs. 5, S4 and S5, all static deformation maps calculated in the $\text{P}\text{--O}\text{--Al}$ planes have very similar ($\pm 0.05 \text{ e \AA}^{-3}$) $\text{P}\text{--O}$ and $\text{Al}\text{--O}$ peak heights, with maximal values of 0.45 and 0.35 e \AA^{-3} , respectively. Similar features were found in X-ray diffraction studies of berlinite (AlPO_4) (Schwarzenbach & Thong, 1979; Porcher *et al.*, 2002). These values are in total disagreement with a theoretical study of berlinite (Corà *et al.*, 2001) that found almost no $\text{Al}\text{--O}$ deformation density, even if we take into account the fact that the reference state in the experimental and theoretical studies is not the same. As already observed in aluminosilicates (for example, in natrolite; Ghermani *et al.*, 1996), the charge-density accumulation close to the O atoms in the $\text{Al}\text{--O}$ bonds confirms that $\text{Al}\text{--O}$ bonds have a more ionic character than $\text{P}\text{--O}$ bonds ($\text{Si}\text{--O}$ in natrolite and topaz; Ivanov *et al.*, 1998).

In the two $\text{Al1}\text{--O9}\text{--Al2}$ planes, the $\text{Al}\text{--O}$ deformation density (Fig. 6a and S6) is polarized towards the Al atoms and exhibits a similar height (0.25 e \AA^{-3}), despite different bond distances (2.04 and 2.18 \AA for the $\text{Al1}\text{--O9}$ and $\text{Al2}\text{--O9}$ bonds, respectively). The O9 deformation density presents two distinct lobes centred on the $\text{Al}\text{--O}$ bonds, which form an open angle (123°) around atom O9. In the $\text{Al1}\text{--O9}\text{--Al1}$

plane, however, where the Al1–O9–Al1 angle is close to 90°, the resulting deformation density has a ‘banana’ shape (Fig. 6*b*), which is also evident from the experimental deformation-density map (Fig. S7). Such a shape has also been observed in α -spodumene (Kuntzinger, 1999) in the Al–O–Al plane [Al–O–Al = 101.12 (1)°].

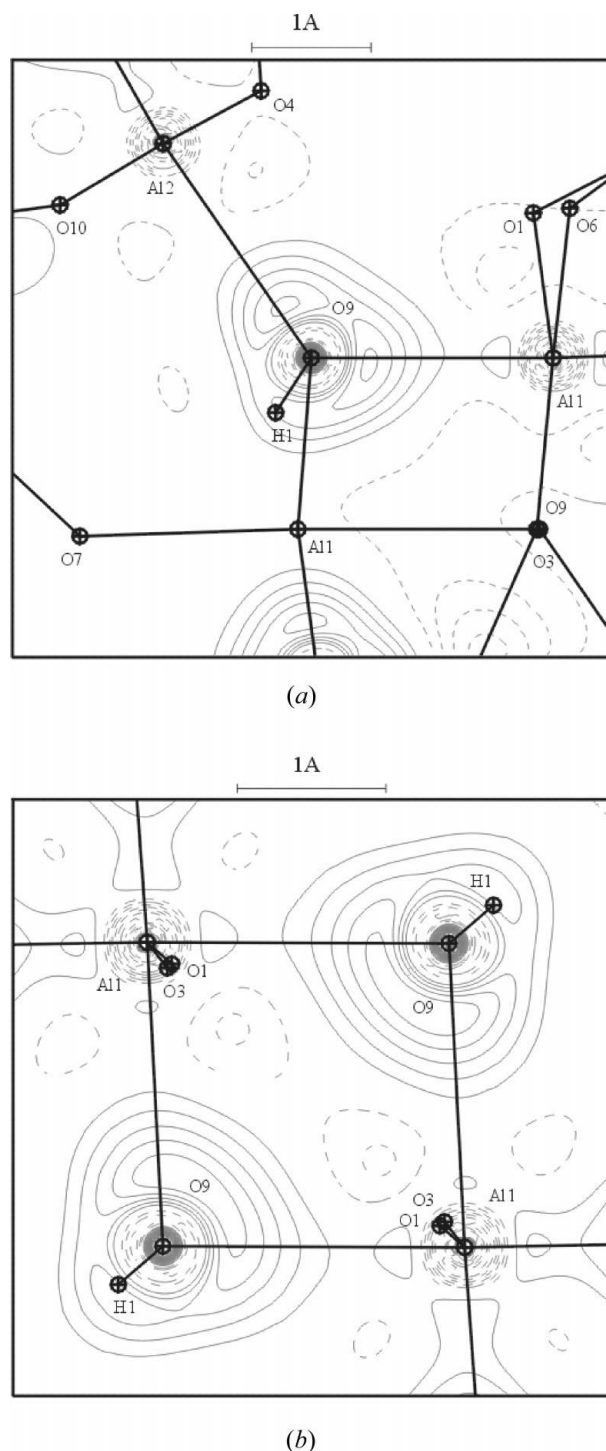


Figure 6
Static deformation maps. (a) Al2–O9–Al1 plane. (b) Al1–O9–Al1 plane. Contours as in Fig. 2.

The oxygen lone-pair density is very well resolved for all O atoms that have a P–O–Al angle smaller than 135° or that are involved in short intermolecular interactions (atoms O1, O3, O4, O5, O6 and O11). When the P–O–Al angle is large (atoms O2 and O8), the corresponding oxygen non-bonding density is not localized. The lone-pair densities of the two water O atoms are very different. Note that the O10-atom lone pair is precisely directed towards atom Al2, to which atom

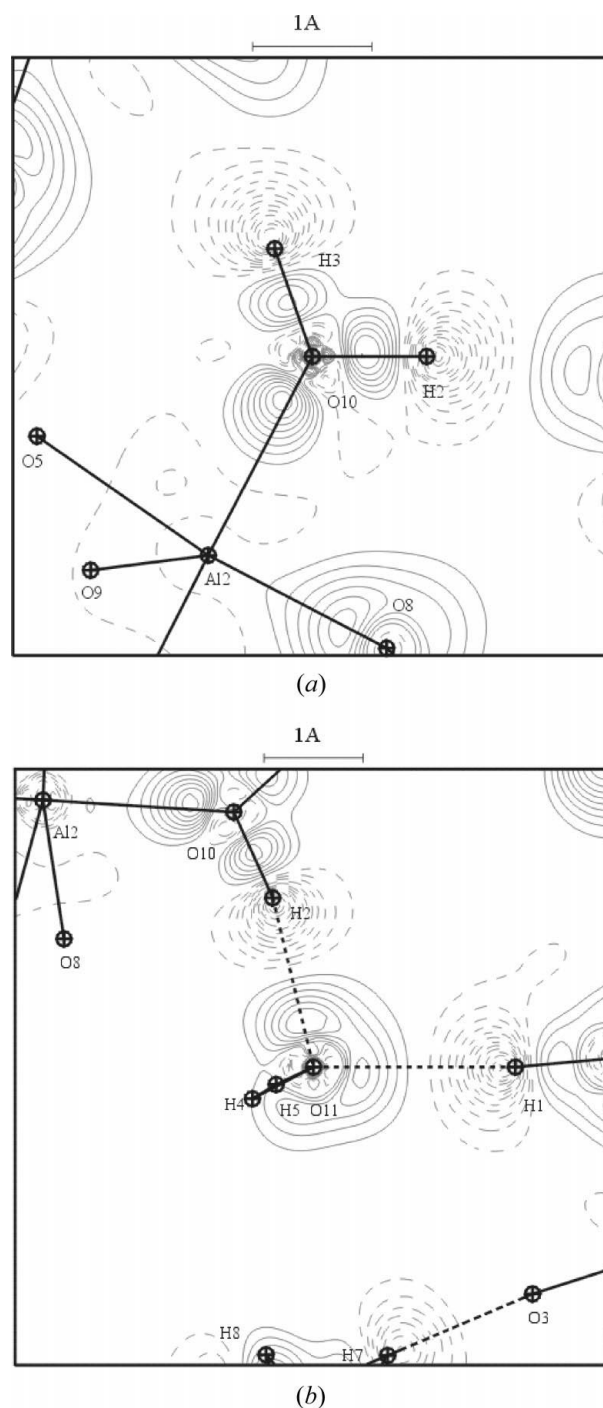


Figure 7
Static deformation maps. (a) H2–O10–H3 plane. Atom Al2 lies 0.47 Å out of this plane. (b) H2–O11–H1 plane. Contours as in Fig. 2.

Table 6

Topological properties of the (3,−1) critical points of the experimental density.

In $M-X$ bonds, d_1 (d_2) is the distance from atom M (X) to the BCP, d_{1-2} is the interatomic $M-X$ distance and ε is the ellipticity at the BCP ($\varepsilon = \lambda_1/\lambda_2 - 1$). Other properties are as defined in the text.

Atom 1–2	d_1 (Å)	d_2 (Å)	d_{1-2} (Å)	$\nabla^2\rho(\mathbf{r}_{\text{cp}})$ (e Å^{-3})	$\rho(\mathbf{r}_{\text{cp}})$ (e Å^{-3})	ε	λ_3 (e Å^{-5})	λ_2 (e Å^{-5})	λ_1 (e Å^{-5})	$(\lambda_1 + \lambda_2)/2$ (e Å^{-5})	$ \lambda_1 + \lambda_2 /2$ ($2 \times \lambda_3$)
P1–O1	0.64	0.91	1.5410 (2)	6.4	1.55	0.06	29.7	−11.3	−12.0	−11.7	0.39
P1–O2	0.63	0.88	1.5101 (2)	8.4	1.67	0.05	33.3	−12.2	−12.8	−12.5	0.38
P1–O3	0.64	0.91	1.5498 (2)	4.6	1.55	0.06	27.4	−11.1	−11.1	−11.1	0.41
P1–O4	0.64	0.91	1.5433 (2)	3.4	1.61	0.04	27.7	−11.9	−12.4	−12.2	0.44
P2–O5	0.63	0.90	1.5326 (2)	6.8	1.59	0.04	30.6	−11.6	−12.1	−11.9	0.39
P2–O6	0.64	0.91	1.5461 (2)	5.0	1.57	0.03	28.7	−11.7	−12.0	−11.9	0.41
P2–O7	0.63	0.90	1.5293 (2)	6.2	1.62	0.05	30.0	−11.7	−12.2	−12.0	0.40
P2–O8	0.63	0.89	1.5204 (2)	8.2	1.63	0.06	32.8	−12.0	−12.7	−12.4	0.38
Al1–O1	0.80	1.07	1.8721 (3)	5.9	0.53	0.05	13.1	−3.6	−3.7	−3.7	0.28
Al1–O3	0.80	1.07	1.8716 (3)	6.8	0.50	0.03	13.7	−3.4	−3.5	−3.5	0.25
Al1–O6	0.80	1.06	1.8567 (2)	6.7	0.53	0.14	14.1	−3.5	−4.0	−3.8	0.27
Al1–O7	0.80	1.06	1.8342 (2)	7.0	0.56	0.09	14.9	−3.8	−4.1	−4.0	0.27
Al1–O9	0.86	1.17	2.0300 (3)	2.8	0.38	0.08	7.3	−2.1	−2.3	−2.2	0.30
Al1–O9	0.86	1.19	2.0479 (3)	3.5	0.34	0.16	7.5	−1.8	−2.1	−2.0	0.26
Al2–O2	0.79	1.06	1.8485 (2)	7.5	0.52	0.10	14.4	−3.3	−3.6	−3.5	0.24
Al2–O4	0.80	1.06	1.8590 (2)	6.0	0.55	0.07	13.6	−3.7	−3.9	−3.8	0.28
Al2–O5	0.79	1.05	1.8330 (2)	7.7	0.55	0.02	15.3	−3.8	−3.9	−3.9	0.25
Al2–O8	0.79	1.04	1.8254 (2)	7.9	0.55	0.05	15.5	−3.7	−3.9	−3.8	0.25
Al2–O9	0.91	1.28	2.1886 (3)	1.8	0.25	0.13	4.3	−1.2	−1.3	−1.3	0.29
Al2–O10	0.82	1.12	1.9415 (3)	5.4	0.42	0.10	10.8	−2.6	−2.9	−2.8	0.25
H1–O9	0.23	0.75	0.987 (5)	−25.7	2.03	0.00	31.9	−28.8	−28.8	−28.8	0.90
H2–O10	0.19	0.77	0.959 (5)	−37.0	2.08	0.03	31.8	−33.9	−34.9	−34.4	1.08
H3–O10	0.20	0.76	0.958 (4)	−36.2	2.13	0.03	31.6	−33.4	−34.3	−33.9	1.07
H4–O11	0.20	0.76	0.957 (4)	−35.0	2.10	0.03	32.1	−33.1	−34.0	−33.6	1.05
H5–O11	0.20	0.76	0.953 (4)	−33.9	2.12	0.02	33.5	−33.3	−34.0	−33.7	1.00
H6–N	0.23	0.77	0.999 (4)	−26.0	1.96	0.02	25.7	−25.7	−26.0	−25.9	1.01
H7–N	0.25	0.75	0.999 (4)	−26.1	2.00	0.01	24.7	−25.3	−25.4	−25.4	1.03
H8–N	0.23	0.76	0.998 (4)	−27.7	1.99	0.01	24.5	−26.2	−26.0	−26.1	1.07
H9–N	0.24	0.76	0.998 (4)	−25.9	1.99	0.01	25.4	−25.8	−25.5	−25.7	1.01

O10 is coordinated (Fig. 7a). Table 5 summarizes the geometrical properties of the $\text{O} \cdots \text{H}$ contacts in $\text{AlPO}_4\text{-15}$ that are defined as hydrogen bonds (see below). The shortest $\text{O} \cdots \text{H}$ interaction is that between the O11 and O10 water molecules ($\text{O11} \cdots \text{H2} = 1.758 \text{ Å}$), which leads to a strong lone-pair polarization towards the H2 atom (Fig. 7b). The other short contacts involve framework O atoms. The O4 and O6 atoms of the framework are involved in two short contacts with their lone pairs directed towards the H atoms of two water molecules (for O6), and one water molecule and one ammonium cation (for O4). In each case, the contacts are asymmetric. The longer contacts (greater than 2.48 Å) involve the multi-connected O2 and O7 framework atoms; consequently, their lone pairs are more diffuse. The only framework atom without an intermolecular contact is O8, which has unresolved lone-pair densities.

3.3. Topological analysis of the charge density

In order to study inter- and intramolecular interactions in a more quantitative way, a topological analysis of the electron

density (Bader, 1990) was performed. The topological properties of a bond critical point (BCP), also called the (3,−1) critical point, are characterized by two negative curvatures (λ_1 and λ_2) in the plane perpendicular to the bond and by one positive curvature (λ_3) along the bond, *i.e.* a minimum of $\rho(\mathbf{r})$ along the bond path. The sum of the λ_i curvatures is the Laplacian [$\nabla^2\rho(\mathbf{r})$] at the BCP, which is a signature of local depletion [$\nabla^2\rho(\mathbf{r}_{\text{cp}}) > 0$] or concentration [$\nabla^2\rho(\mathbf{r}_{\text{cp}}) < 0$] (valence-shell electron concentration, VSEC).

The topology of the total charge density allows partitioning of the atoms. The surface, S , of an atomic basin is defined as $\nabla\rho(\mathbf{r}) \cdot \mathbf{n} = 0$, where \mathbf{n} is a unit vector locally perpendicular to S . Therefore, atomic properties, such as volume, charge and multipole moments, can be derived by integration. All topological calculations were performed using a new version of *NEWPROP* (Souhassou & Blessing, 1999; Souhassou, 2002). The uncertainties on the topological properties cannot be rigorously calculated, but the error on the BCP positions is estimated to be of the order of 0.01 Å , given the electron density. The charge-density error due to the critical-point search is estimated to be 0.01 e Å^{-3} , and the relative uncertainties on λ_i are about 10%. Numerical values at critical points calculated from the multipole model are summarized in Table 6.

The P–O BCPs lie, on average, 0.64 Å from the P atom and 0.90 Å from the O atom. As expected, the P–O density at the BCP is correlated with the bond distance, such that the longer the bond, the lower the density; when P–O increases from 1.51 to 1.55 Å , the charge density at the BCP decreases from 1.67 to 1.55 e Å^{-3} . The positive λ_3 curvature decreases by 18% and, correspondingly, the magnitude of the Laplacian decreases from 8 to 5 e Å^{-5} , remaining slightly positive. The average $|\lambda_1 + \lambda_2|/2\lambda_3$ ratio for P–O bonds (0.40) is close to that for Al–O bonds (0.27). The large charge density at the BCP favours a covalent character for the P–O bonds, but the small positive $\nabla^2\rho(\mathbf{r}_{\text{cp}})$ magnitude and the intermediate value of the curvature ratio suggest a small ionic component. All P–O bonds have an ellipticity close to zero, which indicates cylindrical symmetry along the P–O bond. These conclusions are in line with our previous studies of H_3PO_4 [$\text{P–O} = 1.54 \text{ Å}$ and $\rho(\mathbf{r}_{\text{cp}}) = 1.61 \text{ e Å}^{-3}$, and $\text{P}=\text{O} = 1.49 \text{ Å}$ and $\rho(\mathbf{r}_{\text{cp}}) = 1.73 \text{ e Å}^{-3}$; Souhassou *et al.*, 1995] and NAD^+ [$\text{P–O} = 1.63 \text{ Å}$ and $\rho(\mathbf{r}_{\text{cp}}) = 1.27 \text{ e Å}^{-3}$; Guillot *et al.*, 2003]. A slightly positive Laplacian was also found in both of these studies, as a result of the large λ_3 value. The Al–O bonds have

Table 7

Topological properties of the (3,−1) critical points of the procrystal density.

Caption as in Table 6.

Atom 1–2	d_1 (Å)	d_2 (Å)	d_{1-2} (Å)	$\nabla^2\rho(r_{cp})$ (e Å ^{−3})	$\rho(r_{cp})$ (e Å ^{−3})	ε	λ_3 (e Å ^{−5})	λ_2 (e Å ^{−5})	λ_1 (e Å ^{−5})	$(\lambda_1 + \lambda_2)/2$ (e Å ^{−5})	$ \lambda_1 + \lambda_2 /$ (2 × λ_3)
P1–O1	0.67	0.88	1.5410 (2)	14.0	1.21	0.00	24.8	−5.4	−5.4	−5.4	0.22
P1–O2	0.65	0.86	1.5101 (2)	17.2	1.27	0.00	29.3	−6.1	−6.1	−6.1	0.21
P1–O3	0.67	0.88	1.5498 (2)	13.2	1.19	0.01	23.6	−5.2	−5.2	−5.2	0.22
P1–O4	0.67	0.88	1.5433 (2)	13.8	1.21	0.01	24.5	−5.3	−5.4	−5.4	0.22
P2–O5	0.66	0.87	1.5326 (2)	14.9	1.23	0.00	26.0	−5.6	−5.6	−5.6	0.22
P2–O6	0.67	0.88	1.5461 (2)	13.5	1.20	0.00	24.1	−5.3	−5.3	−5.3	0.22
P2–O7	0.66	0.87	1.5293 (2)	15.2	1.23	0.00	26.5	−5.6	−5.6	−5.6	0.21
P2–O8	0.66	0.86	1.5204 (2)	16.1	1.25	0.00	27.8	−5.8	−5.8	−5.8	0.21
Al1–O1	0.82	1.05	1.8721 (3)	7.4	0.44	0.02	10.9	−1.8	−1.8	−1.8	0.17
Al1–O3	0.82	1.05	1.8716 (3)	7.4	0.44	0.01	10.9	−1.8	−1.8	−1.8	0.17
Al1–O6	0.82	1.05	1.8567 (2)	7.8	0.45	0.02	11.6	−1.9	−1.9	−1.9	0.16
Al1–O7	0.81	1.03	1.8342 (2)	8.6	0.47	0.01	12.7	−2.1	−2.1	−2.1	0.17
Al1–O9	0.89	1.14	2.0300 (3)	3.7	0.34	0.02	5.7	−1.0	−1.0	−1.0	0.18
Al1–O9	0.90	1.15	2.0479 (3)	3.4	0.33	0.02	5.3	−0.9	−1.0	−1.0	0.18
Al2–O2	0.81	1.04	1.8485 (2)	8.1	0.46	0.00	12.0	−1.9	−2.0	−2.0	0.16
Al2–O4	0.82	1.04	1.8590 (2)	7.8	0.45	0.01	11.5	−1.9	−1.9	−1.9	0.17
Al2–O5	0.81	1.03	1.8330 (2)	8.6	0.47	0.00	12.8	−2.1	−2.1	−2.1	0.16
Al2–O8	0.80	1.02	1.8254 (2)	8.9	0.48	0.01	13.2	−2.1	−2.1	−2.1	0.16
Al2–O9	0.98	1.21	2.1886 (3)	1.8	0.27	0.01	3.1	−0.6	−0.6	−0.6	0.19
Al2–O10	0.85	1.09	1.9415 (3)	5.5	0.39	0.05	8.2	−1.3	−1.4	−1.4	0.16
H1–O9	0.22	0.77	0.987 (5)	−10.4	1.66	0.00	31.8	−21.1	−21.1	−21.1	0.66
H2–O10	0.20	0.76	0.959 (5)	−14.1	1.76	0.00	33.9	−24.0	−24.0	−24.0	0.71
H3–O10	0.20	0.76	0.958 (4)	−14.3	1.76	0.00	33.9	−24.2	−24.1	−24.2	0.71
H4–O11	0.20	0.76	0.957 (4)	−14.4	1.76	0.00	34.0	−24.3	−24.2	−24.3	0.71
H5–O11	0.20	0.76	0.953 (4)	−15.1	1.78	0.00	34.3	−24.7	−24.7	−24.7	0.72
H6–N	0.25	0.75	0.999 (4)	−9.1	1.59	0.00	25.5	−17.3	−17.3	−17.3	0.68
H7–N	0.25	0.75	0.999 (4)	−9.0	1.59	0.00	25.4	−17.3	−17.2	−17.3	0.68
H8–N	0.25	0.75	0.998 (4)	−9.1	1.59	0.00	25.5	−17.3	−17.3	−17.3	0.68
H9–N	0.25	0.75	0.998 (4)	−9.1	1.59	0.00	25.5	−17.3	−17.3	−17.3	0.68

Table 8

Comparison of average topological properties calculated from the experimental density and the procrystal data.

Caption as in Table 6. Upper row: multipolar model; lower row: free-atom model.

Atom 1–2	d_1 (Å)	d_2 (Å)	d_2/d_1	$\rho(r_{cp})$ (e Å ^{−3})	λ_3 (e Å ^{−5})	$(\lambda_1 + \lambda_2)/2$ (e Å ^{−5})
P–O	0.64	0.90	1.42	1.60	29.5	−11.9
	0.67	0.88	1.32	1.22	25.6	−5.5
Al–O short	0.80	1.06	1.33	0.54	14.4	−3.8
	0.81	1.04	1.28	0.46	12.0	−2.0
Al1–O9	0.86	1.18	1.37	0.36	7.4	−2.1
	0.90	1.15	1.28	0.34	5.5	−1.0
Al2–O10	0.82	1.12	1.37	0.42	10.8	−2.8
	0.85	1.09	1.28	0.39	8.2	−1.4
Al2–O9	0.91	1.28	1.41	0.25	4.3	−1.3
	0.98	1.21	1.23	0.27	3.1	−0.6

a lower density at the BCP than the P–O bonds, which suggests a more ionic character. The short Al–O_{P–O–Al} ((Al–O) = 1.86 Å) BCPs are characterized by a 0.54 e Å^{−3} charge-density accumulation associated with a positive

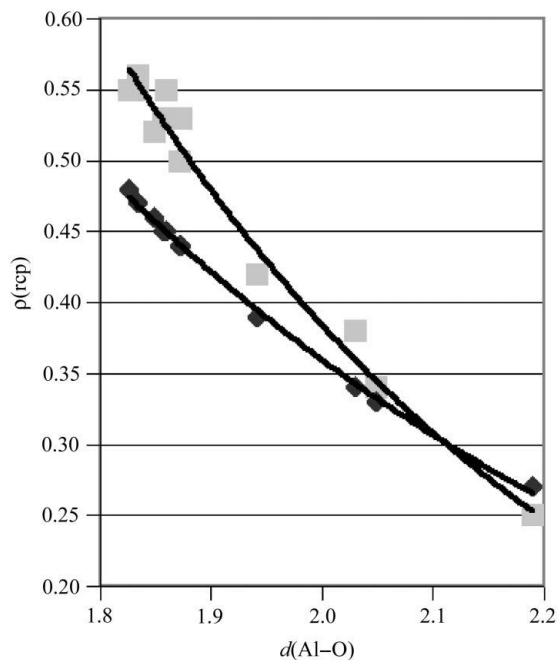
Laplacian (+6.9 e Å^{−3}). These Al–O_{P–O–Al} BCPs lie 0.80 Å from the Al atom and 1.06 Å (d_1 and d_2 in Table 6) from the O atom. For the longer Al–O bonds (1.94 < Al–O < 2.19 Å), the BCP lies closer to the Al atom, as measured by the increasing relative distance d_2/d_1 ; these long Al–O interactions are also characterized by lower charge density and smaller curvatures at the BCPs, *i.e.* less density overlap. In α -spodumene (Kuntzinger, 1999), Al is also octahedrally coordinated and the Al–O BCPs exhibit the same topological features. For the sake of comparison, when Al is tetrahedrally coordinated, the Al–O distances shorten and both $\rho(r_{cp})$ and $\nabla^2\rho(r_{cp})$ increase, as shown in the experimental densities (Kuntzinger *et al.*, 1998, 1999; Kirfel & Gibbs, 2000) or theoretical densities of simple oxides compounds (Hill *et al.*, 1997).

3.4. Comparison with the procrystal

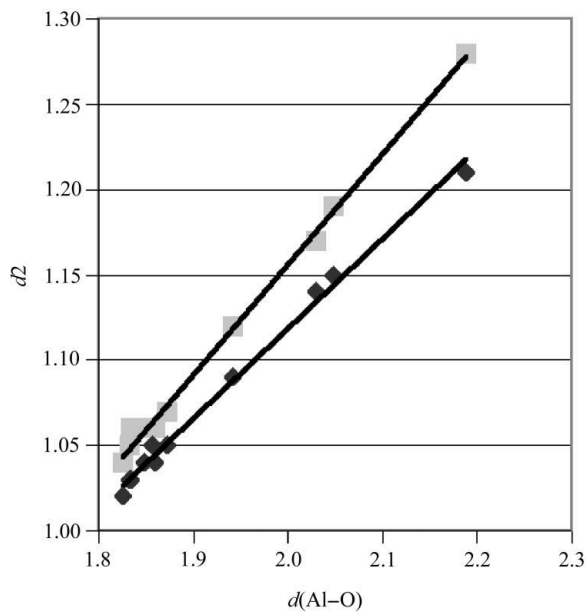
Downs *et al.* (2002) recently published a paper describing the topological properties of such bonds in a procrystal and concluded ‘the procrystal distributions are capable of providing good estimates of the bonded radii of the atoms and the properties of the electron-density distributions at the bond critical points’. As the charge density of AlPO₄-15 presented in the present paper is exceptionally accurate for an inorganic

material, it is interesting to address the conclusion of Downs *et al.* (2002) by comparing the real experimental charge-density parameters with the procrystal parameters. Table 7 shows the topological properties of the procrystal, calculated from the superposition of free-atom electron densities located at the refined positions, and Table 8 compares the average topological properties of P–O and Al–O bonds calculated from the experimental charge density and from the procrystal calculation. In both models, the same Clementi wavefunctions have been used to describe the core and valence densities [equation (1)]. The behaviour of some of the topological properties of Al–O bonds as a function of bonding distance is shown in Fig. 8 for experimental and procrystal densities. Both types of data fit functions of the same nature, *viz.* linear for all values related to P–O, and linear or exponential for Al–O topological values (the linear behaviour for P–O may be linked to the limited range of P–O bond distances compared with that of Al–O). For both P–O and Al–O bonds, the bonded radius of the O atom (d_2) and the perpendicular curvatures increase with the P,Al–O distances, whereas the density at the BCP, the parallel curvature and the Laplacian decrease. In this

way, the gross properties of the bonds are already present in the procrystal representation because of geometrical and core-density effects. However, the procrystal fails to give reliable topological values: inspection of Tables 6–8 shows that the more covalent the bond, the larger the difference between the two models. This trend is expected because a covalent bond,



(a)



(b)

Figure 8

(a) Electron density at Al–O BCPs as a function of Al–O interatomic distances. An exponential fitting curve is superimposed (correlation coefficient > 0.98). (b) Bonded radius of the O atoms (d_2) in the Al–O bonds as a function of Al–O interatomic distances. A linear fitting curve is superimposed (correlation coefficient > 0.99). Grey squares and black diamonds represent the multipolar and procrystal models, respectively.

Table 9

Atomic charges and volumes ($e, \text{\AA}^3$).

Kappa charges are derived from the Kappa refinement (Coppens *et al.*, 1979); topological charges and volumes are derived from the integration of multipolar and procrystal densities over the atomic basins.

Atom	Experimental density				Procrystal model	
	Kappa refinement		Topological		Topological	
	Kappa charge	κ	Charge	Volume	Charge	Volume
P1	1.29 (5)	1.054 (5)	3.45	3.16	2.13	7.01
P2	1.31 (6)		3.48	3.10	2.13	7.94
Al1	1.59 (8)	1.10 (2)	2.43	3.51	1.86	5.18
Al2	1.62 (7)		2.42	3.55	1.86	5.37
O1	−0.88 (2)	0.954 (1)	−1.43	14.89	−0.89	12.83
O2	−0.93 (2)		−1.55	14.72	−0.88	12.59
O3	−0.84 (2)		−1.41	14.18	−0.88	12.23
O4	−0.88 (2)		−1.50	14.16	−0.90	12.00
O5	−0.85 (2)		−1.51	15.35	−0.91	13.25
O6	−0.84 (2)		−1.46	14.32	−0.89	12.02
O7	−0.87 (2)		−1.52	15.16	−0.88	12.72
O8	−0.84 (2)		−1.53	15.54	−0.89	13.23
O9	−0.88 (3)	0.952 (2)	−1.25	12.29	−1.01	11.35
O10	−0.80 (3)	0.959 (2)	−1.40	15.83	−1.01	13.74
O11	−0.68 (3)		−1.15	17.16	−0.83	14.55
N	−0.92 (5)	0.961 (4)	−1.40	17.35	−1.13	15.81
H1	0.56 (3)	1.30 (5)	0.62	1.97	0.35	3.43
H2	0.50 (2)	1.25 (3)	0.66	1.41	0.41	2.79
H3	0.50 (2)		0.66	1.53	0.39	2.98
H4	0.49 (2)		0.65	1.66	0.40	3.27
H5	0.50 (2)		0.64	2.01	0.39	3.67
H6	0.45 (2)	1.25 (3)	0.52	2.44	0.31	3.69
H7	0.45 (2)		0.51	2.52	0.31	3.71
H8	0.45 (2)		0.54	2.26	0.32	3.76
H9	0.47 (2)		0.51	2.53	0.30	3.66

by definition, shares and redistributes electrons. The pertinent parameters to look at are the density at the BCP ($0.4 e \text{\AA}^{-3}$ change in P–O bonds) and the average curvature $[(\lambda_1 + \lambda_2)/2]$ perpendicular to the bond path (54% change). When the ionic character increases, the differences between crystal and procrystal charge densities and perpendicular curvatures at the BCP decrease so as to be almost nullified for the Al₂–O₉ bond. However, in this latter case, the difference lies in the d_2/d_1 ratio, which gives the relative position of the critical point, *i.e.* a measure of the radius of the anion in the ionic-bond direction; this latter value increases with the degree of ionic character. When the multipolar model is used, the O₉-atom bonded radius [$d_2(\text{Al}_2\text{–O}_9)$] increases by 0.07\AA , while the shorter covalent Al–O bonds increase by 0.02\AA ; to a lesser extent, the λ_3 curvature along the ionic bond is also sensitive to charge-density asphericity. This observation is in good agreement with our results on hydrogen-bond topology, where it was found that λ_3 is the pertinent parameter for describing hydrogen-bond strength (Espinosa, Souhassou *et al.*, 1999). Therefore, the conclusion of Downs *et al.* (2002) can be questioned: application of topology to the procrystal does not seem to give a more detailed knowledge than the usual geometrical interpretation. The similarity found by these authors between procrystal and *ab initio* topologies for P–O bonds is surprising; Downs *et al.* (2002) suggested that it may be due to the limited basis sets used in these calculations, which may be unable to reproduce the polarization of the

Table 10

Topological properties of hydrogen bonds.

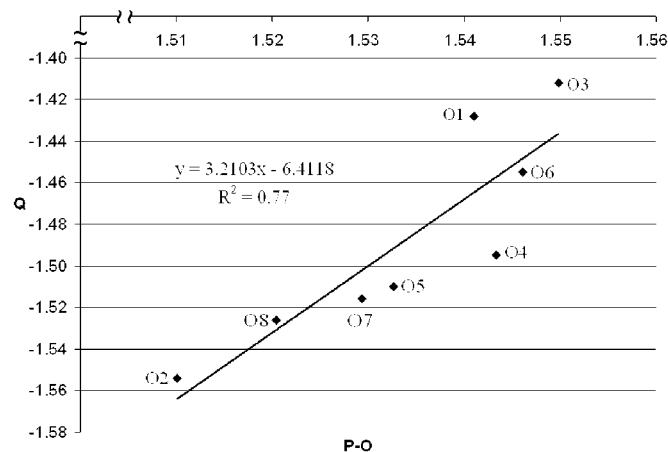
Caption as in Table 6.

$D-H \cdots A$	d_1 (Å)	d_2 (Å)	$\nabla^2 \rho(r_{sp})$ ($e \text{ \AA}^{-5}$)	$\rho(r_{sp})$ ($e \text{ \AA}^{-3}$)	ε	λ_3 ($e \text{ \AA}^{-5}$)	λ_2 ($e \text{ \AA}^{-5}$)	λ_1 ($e \text{ \AA}^{-5}$)	G (kJ mol^{-1} per a.u. vol.)	V (kJ mol^{-1} per a.u. vol.)	E_e (kJ mol^{-1} per a.u. vol.)
O10–H2···O11	0.58	1.18	3.9	0.24	0.01	6.4	–1.2	–1.2	100 (11)	–93 (12)	7 (8)
	0.67	1.09	3.1	0.33	0.01	6.3	–1.6	–1.6	106 (11)	–128 (13)	–22 (8)
N–H8···O1	0.61	1.21	3.4	0.21	0.11	5.4	–0.9	–1.0	84 (10)	–76 (10)	8 (7)
	0.70	1.12	2.8	0.29	0.04	5.5	–1.4	–1.4	91 (10)	–107 (12)	–16 (7)
N–H6···O5	0.65	1.22	2.9	0.20	0.02	4.7	–0.9	–0.9	74 (9)	–69 (10)	5 (6)
	0.73	1.14	2.6	0.27	0.07	4.9	–1.1	–1.2	81 (9)	–93 (11)	–11 (7)
O11–H4···O4	0.65	1.24	3.1	0.15	0.06	4.4	–0.7	–0.7	69 (8)	–54 (9)	15 (6)
	0.74	1.15	2.5	0.26	0.03	4.8	–1.1	–1.2	77 (9)	–87 (11)	–10 (7)
N–H7···O3	0.65	1.24	3.0	0.17	0.06	4.5	–0.7	–0.8	70 (9)	–59 (9)	11 (6)
	0.74	1.15	2.5	0.26	0.06	4.8	–1.1	–1.2	78 (9)	–88 (11)	–10 (7)
O10–H3···O6	0.66	1.26	2.9	0.14	0.16	4.2	–0.6	–0.7	65 (8)	–50 (8)	14 (5)
	0.75	1.15	2.4	0.25	0.04	4.6	–1.1	–1.1	75 (9)	–84 (11)	–9 (6)
N–H9···O4	0.73	1.29	2.2	0.15	0.09	3.5	–0.6	–0.6	54 (7)	–47 (8)	7 (5)
	0.80	1.20	2.1	0.21	0.10	3.7	–0.7	–0.8	61 (8)	–65 (9)	–4 (6)
O9–H1···O11	0.68	1.36	2.5	0.07	0.08	3.0	–0.3	–0.3	49 (6)	–31 (6)	18 (4)
	0.83	1.20	1.9	0.18	0.03	3.4	–0.7	–0.8	53 (7)	–54 (8)	–1 (5)
O11–H5···O6	0.74	1.34	2.0	0.11	0.09	2.8	–0.4	–0.4	44 (6)	–33 (7)	11 (4)
	0.84	1.23	1.8	0.18	0.07	3.1	–0.6	–0.7	51 (7)	–52 (8)	–1 (5)
O10–H3···O7	1.06	1.50	0.9	0.06	1.02	1.2	–0.1	–0.2	20 (3)	–15 (4)	5 (2)
	No CP found										
N–H6···O2	1.13	1.44	1.1	0.08	1.78	1.4	–0.1	–0.3	24 (4)	–19 (5)	5 (3)
	1.10	1.39	1.1	0.09	3.80	1.4	–0.1	–0.3	26 (4)	–21 (5)	4 (3)
O11–H4···O2	1.11	1.48	1.0	0.07	0.64	1.3	–0.1	–0.2	21 (4)	–16 (4)	5 (3)
	No CP found										
N–H8···O7	1.13	1.48	0.8	0.06	0.64	1.2	–0.1	–0.2	18 (3)	–13 (4)	5 (2)
	No CP found										
O11–H5···O7	1.14	1.55	0.7	0.04	0.54	0.9	–0.1	–0.1	13 (2)	–9 (3)	4 (2)
	No CP found										

atoms. Therefore, accurate charge-density measurements are much more consistent and should be performed in order to better understand the bonding properties of zeolite-like systems.

3.5. Atomic and molecular net charges

Table 9 gives the atomic charges as calculated for a Kappa refinement ($q = N_v - P_v$) and from integration over the

**Figure 9**

Topological charges of O_{P-O-Al} atoms, derived from the multipolar refinement, plotted as a function of the P–O distances (in Å). The best linear fit ($R^2 = 0.77$) is displayed in the figure.

atomic basins (topological charges). For the sake of comparison, procrystal topological charges are also displayed. For all atoms, the topological charges are larger than the Kappa charges, as is usually observed. Both methods, however, give accurate results in the sense that chemically equivalent atoms bear the same charge: the P and Al topological charges are +3.47 (2) and +2.43 (1), respectively [+1.30 (1) and +1.61 (2) for Kappa charges]. The P and Al topological charges are closer to the formal oxidation numbers V (P) and III (Al). The topological charges of the O_{P-O-Al} atoms are related to the P–O bond lengths: the larger the O-atom charge, the shorter the bond, as illustrated in Fig. 9. Such a relation is not evident for procrystal topological charges or Kappa charges. P–O bond lengths and O-atom topological charges are correlated with the Al–O–P angles: the larger the P–O–Al angles, the more negative the O-atom charges. This behaviour is in line with the results of theoretical calculations for small $[(H_nX)_2O]$ molecules reported by Gillespie & Johnson (1997), but not with the results of Gibbs *et al.* (1997) who argue that as the interatomic distance increases in Si–O bonds, the bonded radius of the oxide anions increases together with the atomic charge. Relations between Mulliken charges for O atoms and geometrical properties ($M-O$ bond lengths and $M-O-M'$ angles) were also derived for all-siliceous and aluminophosphate zeolites by Larin & Vercauteren (1998, 2001).

The H_2O and OH topological charges agree in the chemical sense: charge transfer occurs from the Al atom to the coordinated OH and H_2O groups, which are negatively charged

(−0.63 and −0.07, respectively, compared with +0.14 for the O11 water molecule). The corresponding values for the Kappa refinement are −0.32, +0.20 and +0.31. The NH₄ Kappa charge (+0.90) is closer to the formal charge than the topological charge (+0.68). Integrated properties derived from the procrystal model give the right sign for the atomic charges (positive for Al, P and H, and negative for O and N), but the magnitudes totally disagree with those derived from the aspherical model. The P, Al and O_{P–O–Al} procrystal values are, however, in surprisingly close agreement with Mulliken charges calculated on molecular sieves (Larin & Vercauteren, 2001).

In conclusion, multipole integrated properties are in total agreement in the chemical sense: a charge build up and an increase of the anionic volumes are observed, and correspondingly the cations volumes decrease by 30–50%. These properties also account for hydrogen-bond interactions (see below).

3.6. Hydrogen-bonding and intermolecular interactions

Table 10 shows the topological properties of the 14 O···H contacts for which unambiguous (3,−1) BCPs were found between the H and the O atoms. These properties were calculated from the multipolar and procrystal models; in the latter case, some weak O···H contacts were not characterized by a (3,−1) BCP. For the medium and strong hydrogen bonds, the positions of the BCPs derived from the multipolar representation differ from the positions obtained with the procrystal; the multipolar model shifts the BCP towards the H atom, and the resulting charge density at the critical point decreases.

The two hydrogen-bond categories previously established from hydrogen-bond distances (H···A < 2.1 Å and H···A > 2.5 Å) are distinguished from the Laplacian and the density at the critical points: $\rho(\mathbf{r}_{\text{cp}})$ is large for short bonds and *vice versa*. Only H1···O11, which concerns the O9/H1 hydroxyl group, exhibits a low density (0.07 e Å^{−3}) at the BCP, despite a relatively short distance (2.04 Å).

As observed in a previous study (Pluth *et al.*, 1984), H···O bond distances (Table 5) seem to be correlated to P–O and Al–O bond lengths (Table 4); in general, the longest P,Al–O distances are observed for O atoms involved in a short hydrogen bond.

The strength of the hydrogen bonds can be evaluated by computing the kinetic (*G*), potential (*V*) and total (*Ee*) energy densities at the critical point using the Abramov equation (Abramov, 1997) (in atomic units)

$$G(r_{\text{cp}}) = (3/10) (3\pi^2)^{2/3} \rho^{5/3}(r_{\text{cp}}) + \nabla^2 \rho(r_{\text{cp}})/6, \quad (4)$$

the virial equation

$$2G(r) + V(r) = \nabla^2 \rho(r)/4, \quad (5)$$

and

$$Ee(r) = G(r) + V(r). \quad (6)$$

Note that the Abramov formula is only valid for the exact electron density and is approximately valid for multipolar

density. An application to procrystal density is, by nature, questionable.

Following previous work (Espinosa, Lecomte & Molins, 1999; Espinosa, Souhassou *et al.*, 1999), the kinetic and potential energy densities at hydrogen-bond BCPs were fitted against the longitudinal (λ_3) and perpendicular (λ_1 and λ_2) curvatures (λ_i in e Å^{−5}), respectively, for both multipolar and procrystal models. The *G* and *V* (kJ mol^{−1} per atomic unit volume) expressions obtained are $G = 15.7\lambda_3$ and $16.5\lambda_3$, and $V = 39.0(\lambda_1 + \lambda_2)$ and $39.1(\lambda_1 + \lambda_2)$ for the multipolar and procrystal models, respectively. The results from the procrystal model are similar to those obtained from the multipolar analysis (for each fitting, correlation factors are greater than 0.98) and are close to that of Espinosa, Lecomte & Molins (1999). The exponential behaviour of *G* and *V* versus H···A (Fig. 10) and the differences between the procrystal and multipolar models are similar to those reported in previous studies (Espinosa *et al.*, 1998; Spackman, 1999). As shown in the latter paper, the procrystal model is able to give the global trends in the characteristics of the hydrogen-bond BCPs, but only a more sophisticated model (like the multipolar model) can take into account detailed features of the hydrogen bonds, such as the features responsible for the systematic differences between the $\rho(\mathbf{r}_{\text{cp}})$, $d_{1,2}$ and *V* parameters. However, even if a very precise multipolar density is available (as in this study), it is not straightforward to establish and rationalize relationships among asymmetries observed in bond lengths and BCP properties. These difficulties may arise from the fact that in minerals there is no clear spatial distinction between intra- and intermolecular interactions, as there is in molecular crystals.

4. Conclusion

An accurate charge-density analysis of the AlPO₄-15 molecular sieve has been presented, from which clear interatomic interactions are revealed. From the comparison of topological

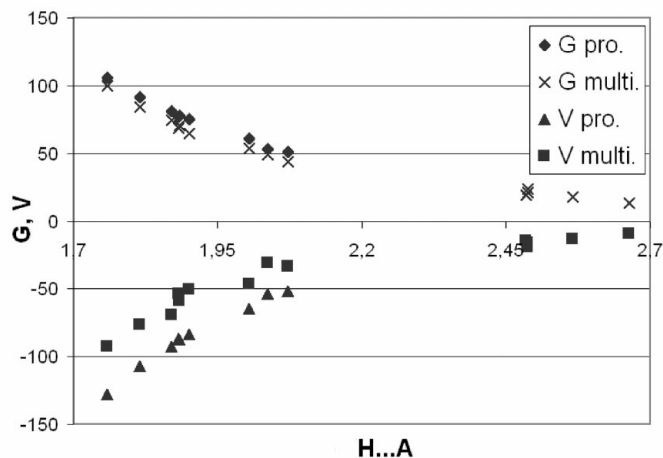


Figure 10 Kinetic (*G*) and potential (*V*) energy densities at hydrogen-bond BCPs for the multipolar and procrystal models as a function of H···A interatomic distances (*G* and *V* in kJ mol^{−1} per atomic unit volume and H···A in Å).

properties derived from the procrystal and multipolar models, we have shown that the procrystal is able to provide global trends (the sign of atomic charges and the variations of topological properties with geometrical characteristics), but not the correct magnitudes. In the case of predominantly covalent bonds (P–O), the main differences between the two models lie in the density and the curvatures at the BCP. With increasing ionic character (Al–O bonds), these differences decrease, while the discrepancies in the bonded radius of the O atoms increase. The O-atom topological charges derived from the multipolar model are related to simple geometrical characteristics (P–O bond length and P–O–Al angle), which is contrary to the procrystal results. As noted for Mulliken charges by Larin & Vercauteren (2001), such a relation can be exploited in order to estimate charges/multipoles and then electrostatic properties for interesting molecular sieves for which theoretical/experimental charge densities are currently inaccessible. Systematic studies of topological charges and their relations to geometric characteristics are first required. The multipolar model makes more chemical sense than a simple procrystal model, but some points, such as variations of Laplacian and topological atomic charges with bond length, are still to be clarified.

It would be interesting to compare deformation densities and topological properties derived from theoretical calculations and experimental results. In a forthcoming paper, electrostatic properties will be derived from the charge density of this compound, from which binding energies of the molecules trapped inside the molecular sieve (water molecules, ammonium and hydroxyl ions) can be estimated. Examination of the topological properties of the electrostatic potential is also of interest, as it can provide another viewpoint on the interatomic interactions and gives access to the derivatives of the potential felt by the molecules.

The authors are grateful to J. Reymann and C. Palin for their technical help and to A. Clause-Gulia for her work on the manuscript. AE is grateful to the Ministère de la Jeunesse, de l'Éducation Nationale et de la Recherche, France, for a doctoral fellowship.

References

- Abramov, Y. A. (1997). *Acta Cryst.* **A53**, 264–272.
- Allen, F. H., Kennard, O., Watson, D. G., Brammer, L., Orpen, A. G. & Taylor, R. (1987). *J. Chem. Soc. Perkin Trans. 2*, pp. S1–19.
- Bader, R. F. W. (1990). *Atoms in Molecules: A Quantum Theory*. Oxford: Clarendon Press.
- Becker, P. J. & Coppens, P. (1974). *Acta Cryst.* **A30**, 129–153.
- Beitone, L., Loiseau, T. & Férey, G. (2002). *Acta Cryst.* **C58**, i103–i105.
- Blessing, R. H. (1989). *J. Appl. Cryst.* **22**, 396–397.
- Blessing, R. H. (1997). *J. Appl. Cryst.* **30**, 421–426.
- Blessing, R. H., Guo, D. Y. & Langs, D. A. (1998). *Intensity Statistics and Normalization in Direct Methods for Solving Macromolecular Structures*, edited by S. Fortier, pp. 47–71. Dordrecht: Kluwer Academic Publishers.
- Brünger, A. T. (1992). *Nature (London)*, **355**, 472–475.
- Cheetham, A. K., Férey, G. & Loiseau, T. (1999). *Angew. Chem. Int. Ed.* **38**, 3268–3292.
- Clementi, E. & Roetti, C. (1974). *At. Data Nucl. Data Tables*, **14**, 177–478.
- Coppens, P., Guru Row, T. N., Leung, P., Stevens, E. D., Becker, P. J. & Yang, Y. W. (1979). *Acta Cryst.* **A35**, 63–72.
- Corà, F., Catlow, C. R. A. & D'Erocle, A. (2001). *J. Mol. Catal. A: Chem.* **166**, 87–99.
- DeTitta, G. T. (1985). *J. Appl. Cryst.* **18**, 75–79.
- Dick, S. & Zeiske, T. (1997). *J. Solid State Chem.* **133**, 508–515.
- Downs, R. T., Gibbs, G. V., Boisen, M. B. Jr & Rosso, K. M. (2002). *Phys. Chem. Miner.* **29**, 369–385.
- Espinosa, E., Lecomte, C. & Molins, E. (1999). *Chem. Phys. Lett.* **300**, 745–748.
- Espinosa, E., Molins, E. & Lecomte, C. (1998). *Chem. Phys. Lett.* **285**, 170–173.
- Espinosa, E., Souhassou, M., Lachekar, H. & Lecomte, C. (1999). *Acta Cryst.* **B55**, 563–572.
- Gabe, E. J., Lepage, Y., Charland, J. P., Lee, F. L. & White, P. S. (1989). *J. Appl. Cryst.* **22**, 384–387.
- Ghermani, N. E., Lecomte, C. & Dusausoy, Y. (1996). *Phys. Rev. B*, **53**, 5231–5239.
- Gibbs, G. V., Hill, F. C. & Boisen, M. B. Jr (1997). *Phys. Chem. Miner.* **24**, 167–178.
- Gillespie, R. J. & Johnson, S. A. (1997). *Inorg. Chem.* **36**, 3031–3039.
- Guillot, B., Muzet, N., Jelsch, C., Artacho, E. & Lecomte, C. (2003). *J. Phys. Chem. B*. Submitted.
- Guillot, B., Viry, L., Guillot, R., Lecomte, C. & Jelsch, C. (2001). *J. Appl. Cryst.* **34**, 214–223.
- Hansen, N. K. (1998). *Internal Software LCM³B*. Université Henri Poincaré – Nancy, France.
- Hansen, N. K. & Coppens, P. (1978). *Acta Cryst.* **A34**, 909–921.
- Hill, F. C., Gibbs, G. V. & Boisen, M. B. Jr (1997). *Phys. Chem. Miner.* **24**, 582–596.
- Ivanov, Y. V., Belokoneva, E. L., Protas, J., Hansen, N. K. & Tsirelson, V. G. (1998). *Acta Cryst.* **B54**, 774–781.
- Jelsch, C., Teeter, M. M., Lamzin, V., Pichon-Pesme, V., Blessing, R. H. & Lecomte, C. (2000). *Proc. Natl Acad. Sci. USA*, **97**, 3171–3176.
- Johnson, C. K. (1976). *ORTEPII*. Report ORNL-5138. Oak Ridge National Laboratory, Tennessee, USA.
- Kirfel, A. & Gibbs, G. V. (2000). *Phys. Chem. Miner.* **27**, 270–284.
- Kissel, L., Zhou, B., Roy, S. C., Sen Gupta, S. K. & Pratt, R. H. (1995). *Acta Cryst.* **A51**, 271–288. (<http://www-Phys.llnl.gov/Research/scattering/index.html>.)
- Kuntzinger, S. (1999). PhD thesis, Université Henri Poincaré – Nancy, France.
- Kuntzinger, S., Dahaoui, S., Ghermani, N. E., Lecomte, C. & Howard, J. A. K. (1999). *Acta Cryst.* **B55**, 867–881.
- Kuntzinger, S. & Ghermani, N. E. (1999). *Acta Cryst.* **B55**, 273–284.
- Kuntzinger, S., Ghermani, N. E., Dusausoy, Y. & Lecomte, C. (1998). *Acta Cryst.* **B54**, 819–833.
- Larin, A. V. & Vercauteren, D. P. (1998). *Int. J. Quant. Chem.* **70**, 993–1001.
- Larin, A. V. & Vercauteren, D. P. (2001). *J. Mol. Catal. A: Chem.* **166**, 73–85.
- Nonius (1997). *KappaCCD Software*. Nonius BV, Delft, The Netherlands.
- Nandini Devi, R. & Vidyasagar, K. (1999). *J. Chem. Soc. Dalton Trans.* pp. 3841–3845.
- Otwinowski, Z. & Minor, W. (1997). *Methods in Enzymology*, Vol. 276, *Macromolecular Crystallography*, Part A, edited by C. W. Carter Jr & R. M. Sweet, pp. 307–326. New York: Academic Press.
- Péres, N. (1997). PhD thesis, University H. Poincaré Nancy I, France.
- Péres, N., Souhassou, M., Wyncke, B., Gavaille, G., Cousson, A. & Paulus, W. (1997). *J. Phys. Condens. Mater.* **9**, 6555–6562.
- Pichon-Pesme, V., Lecomte, C. & Lachekar, H. (1995). *J. Phys. Chem.* **99**, 6242–6250.
- Pluth, J. J., Smith, J. V., Bennett, J. M. & Cohen, J. P. (1984). *Acta Cryst.* **C40**, 2008–2011.

- Porcher, F., Larin, A. V., Aubert, E., Vercauteren, D. P., Souhassou, M., Lecomte, C. & Philippot, E. (2002). Isomorphous substitution in XIIIYVO_4 compounds and related electrostatic properties by experimental/theoretical modelling of crystal electron density: from low quartz isostructural compounds to zeolites. EURESCO Conf. on Molecular Sieves, Obernai, France.
- Schwarzenbach, D. & Thong, N. (1979). *Acta Cryst.* **A35**, 652–658.
- Souhassou, M. (2002). *Internal Software LCM³B*. Université Henri Poincaré – Nancy, France.
- Souhassou, M. & Blessing, R. H. (1999). *J. Appl. Cryst.* **32**, 210–217.
- Souhassou, M., Espinosa, E., Lecomte, C. & Blessing, R. H. (1995). *Acta Cryst.* **B51**, 661–668.
- Spackman, M. A. (1999). *Chem. Phys. Lett.* **301**, 425–429.
- Stewart, R. F., Davidson, E. R. & Simpson, W. T. (1965). *J. Chem. Phys.* **42**, 175–187.
- Szostak, R. (1992). In *Handbook of Molecular Sieves*. New York: Van Nostrand Reinhold.
- Weiß, Ö., Ihlein, G. & Schüth, F. (2000). *Microporous Mesoporous Mater.* **35–36**, 617–620.